Pulse width dependence of magnetic field generation using laser-powered capacitor coils

View Online   Export Citation   CrossMark

Abraham Chien,[1,a] [ID] Lan Gao,[1] [ID] Shu Zhang,[2] [ID] Hantao Ji,[1] [ID] Eric Blackman,[3] [ID] Hui Chen,[4] [ID]
Gennady Fiksel,[5] [ID] Kenneth Hill,[1] [ID] and Philip Nilson[6]

AFFILIATIONS

[1]Princeton Plasma Physics Laboratory, Princeton University, Princeton, New Jersey 08543, USA
[2]Department of Astrophysical Sciences, Princeton University, Princeton, New Jersey 08544, USA
[3]University of Rochester, Rochester, New York 14627, USA
[4]Lawrence Livermore National Laboratory, Livermore, California 94550, USA
[5]University of Michigan, Ann Arbor, Michigan 48109, USA
[6]Laboratory for Laser Energetics, University of Rochester, Rochester, New York 14623, USA

[a]Author to whom correspondence should be addressed: achien2@pppl.gov

ABSTRACT

Megagauss magnetic fields were generated by a current flowing through a U-shaped coil connecting two parallel copper foils. Two kJ-class lasers at various pulse widths from 2 ns to 9.9 ns passed through holes in the front foil and were focused on the back foil with an intensity of $\sim 1.7 \times 10^{16}$ W/cm^2. The coil current and resulting magnetic fields were characterized using ultrafast proton radiography, timed at the end of the laser pulses. The measurements show that magnetic field strength decays with increasing laser pulse width. A lumped-circuit model was developed and showed consistency with the experimental measurements, demonstrating an *ion shorting* effect: as the ion current neutralizes the electron current contribution to interplate voltage, the coil current peaks on a timescale close to the ion transit time $t_i = d/v_{ion}$. FLASH simulations of the coil current are performed, and the calculated resistance values are used to constrain ion speed as a function of hot electron temperature.

I. INTRODUCTION

The study of strongly magnetized high energy density (HED) plasmas is an active enterprise of research across multiple platforms. The capability to impose strong quasistatic magnetic fields in the laboratory opens up significant possibilities. Ongoing research efforts include direct-drive ICF,[1] magnetic reconnection,[2,3] collisionless shocks,[4] and hohlraum plasma magnetization in indirect-drive inertial fusion,[5] to name a few. Recently, a robust platform for generating strong external magnetic fields has emerged using intense lasers and a unique capacitor-coil target. First introduced by Korobkin[6] in 1979, the technique has been developed by many groups[2,7–18] and provides a reliable method to generate up to kiloTesla magnetic fields.[19,20] The capacitor coil targets are typically composed of two parallel metallic plates (the capacitor) connected with thin wire(s) in different geometric shapes (the coil). Hot electrons are generated as the laser beam hits the back plate,[21,22] building up a voltage difference between the front

and back plates and driving a large current through the connecting coil. This large current results in strong magnetic field generation.

The optimization of magnetic field generation using this platform is an ongoing effort. Typically, capacitor-coil targets are driven for $\sim$1 ns in order to maximize laser intensity, and by extension, the generated hot electron temperature. Short laser drive, however, may limit current generation, as the current rise rate occurs on order the L/R time (where L is coil inductance and R is resistance), which is often larger than the laser drive time. Increasing the drive time while only slightly sacrificing laser intensity, therefore, may potentially result in a stronger magnetic field. This work investigates the effect of increasing laser pulse width on magnetic field generation, backed up by a lumped-circuit model to understand the underlying physics mechanisms.

A few studies[6,17,18,23] drove capacitor coils using longer ($>$1 ns) laser pulse durations, but most do not clearly study the pulse length

effect on current generation. In 2020, Williams et al.[18] found an increase in maximum coil current with increasing laser pulse width, up to 10 ns. The coil current was reported to rise, even past the laser shut-off time, and eventually saturate. A plasma diode model was applied and proved successful in predicting experimentally measured current and voltage traces. Williams et al.[18] studied laser energies in the 0.001–30 J range at intensities of 10^9–10^{13} W/cm^2, while this study focuses on kJ-scale laser energies and laser intensity in the 10^{16} W/cm^2 range. At these higher energies and intensity, strong plasma flows are generated between the capacitor plates, and the plasma diode model is not directly applicable.

The paper is organized as follows. Section II describes the experimental setup. Section III presents the experimental results and interpolation of the experimental observations using proton ray tracing calculations. Section IV presents our lumped-circuit model and its relevance to our experimental results. Time-dependent effects, particularly affecting wire resistance, are investigated. Section V provides a discussion on the application of the lumped-circuit model and constraints on the allowed hot electron temperature and ion velocities are obtained using the lumped-circuit model. An explanation of the outer bubble feature in proton radiographs is also included in this section. Section VI summarizes the results and future work based on this study. Acknowledgments and a data availability statement follow.

II. EXPERIMENTAL SETUP

The experiments were conducted on the OMEGA EP Laser System at the Laboratory of Laser Energetics, University of Rochester. Two EP long pulse beams [351 nm wavelength (3ω)] were used to drive the main interaction with a combined intensity of $\sim 1.7 \times 10^{16}$ W/cm^2 on target. A laser pulse duration scan was conducted with square pulse widths of 2, 3, 4, 9.9 ns, at combined laser energies of 2.88, 4.32, 5.76, and 10.2 kJ, respectively, to maintain constant intensity. A schematic of the target chamber geometry is shown in Fig. 1.
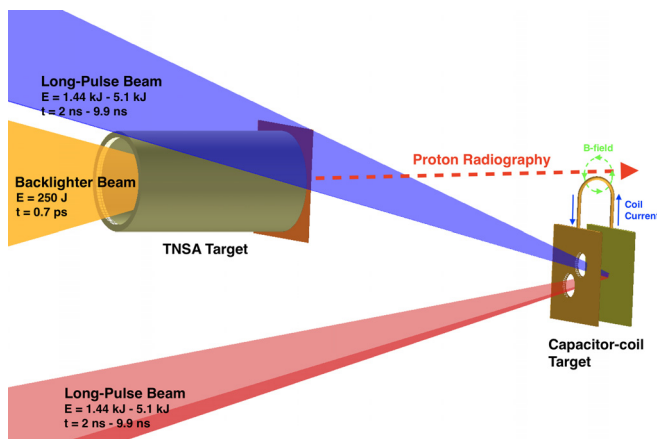

FIG. 1. Experimental setup on OMEGA EP. As the EP long-pulse beams irradiate the back Cu plate and build a voltage between the two parallel plates, strong currents are generated in the coil, creating a strong magnetic field. A short-pulse backlighter beam hitting the TNSA target generates high-energy protons that probe the electromagnetic field structure at the capacitor-coil target.

The capacitor-coil targets are made of two parallel Cu plates (square, 1500 μm length, 50 μm thickness), spaced 600 μm apart and connected by a centered U-shaped Cu coil (rectangular cross section, 100 μm $\times$50 μm thickness). The U-shaped coils are comprised of two parallel straight sections of 500 μm length connected with a semi-circle with radius 300 μm. Two laser entrance holes are cut from the front plate, allowing the long-pulse beams to pass through and focus onto the back plate. These lasers irradiate the rear plate, generating a beam of hot electrons. These hot electrons stream onto the front plate and build up an electric potential between the plates, creating a large current flowing through the coils from the back plate toward the front plate, and generating strong magnetic fields around the coil.

Electromagnetic fields were diagnosed with TNSA (target normal sheath acceleration)[24] proton radiography. A wideband distribution of high-energy protons (up to 60 MeV) is generated[25] by irradiating a 20 μm-thick Cu foil with the 250 J, 0.7 ps OMEGA EP backlighter. The energetic protons stream $\sim$7 mm toward the main interaction target coil region. The Lorentz force from local electromagnetic fields deflects the protons, and they are finally deposited onto a radiochromic film (RCF) pack $\sim$80 mm from the coil region. The RCF pack is composed of alternating layers of Al filters and films, allowing measurement at various proton energies. In all cases, the backlighter beam was timed to 15 ps before the end of the long-pulse irradiation. Accounting for proton travel time from the TNSA target to the capacitor-coil target, this allowed for consistent diagnosis of the electromagnetic fields at the end of the laser pulse.

III. EXPERIMENTAL RESULTS

Proton radiographs were taken of the target region immediately after turning off the long-pulse beams. Taking into account time-of-flight for the energetic protons to reach the target area, the radiographs represent field measurements at $t = 0.027$, 0.014, 0.007, and 0.027 ns with respect to the end of the square pulse, for pulse widths of 2, 3, 4, and 9.9 ns, respectively. Variations in the field measurement timings are small compared to the laser pulse widths as well as the typical current decay time ($\sim$10 ns[3]) Therefore, differences in probe time are not expected to meaningfully affect the analysis and conclusions. Experimental radiographs for proton energy of 24.7 MeV are shown in Fig. 2. The primary feature is the formation of a prolate void, generated by the magnetic field from the driven coil current. It is important to note that the prolate void that represents the deflection from the coil-generated magnetic field is the inner lighter structure, not the outer structure formed by caustics. The outer structures are formed by a return current and are discussed further in Sec. V.

To determine magnetic field strength, synthetic radiographs are generated via a particle ray-tracing code. Local magnetic fields are calculated with the Biot-Savart law. To calculate the coil-generated magnetic field, the semicircular coil is discretized into 50 equal-length current-carrying segments. The magnetic field from the coils is computed for vertices in a cubic mesh (2.5 mm side length, 5 μm mesh size) centered around the coil region. A quiver plot representation of the calculated magnetic field is shown in Fig. 3. In the ray-tracing simulation, protons are advanced via a fourth-order adaptive Runge–Kutta algorithm. At each time step, the local fields are calculated at the proton location using tri-linear interpolation from the electromagnetic field mesh.
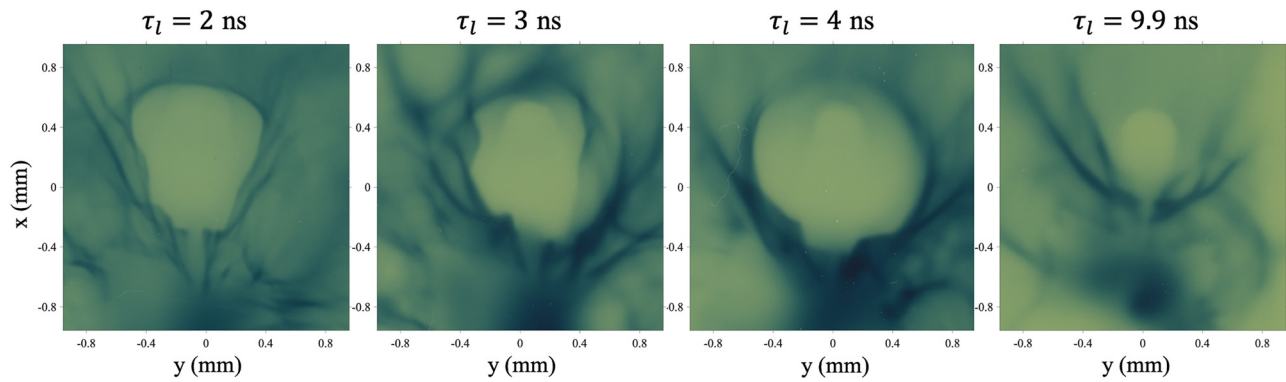
FIG. 2. Experimental proton radiographs for laser pulse widths of $\tau_l = 2, 3, 4$, and 9.9 ns. Laser intensity is the same for all shots at 1.7×10^{16} W/cm^2. Two primary features are observed: an inner lighter feature representing deflection by the coil-generated magnetic field and an outer ring bordered by caustics caused by the return current. The outer feature is discussed further in Sec. V. Here, $E_p = 24.7$ MeV.

The size of the prolate voids created by the U-shaped coils has been shown to scale as $r \propto I^{0.5}E_p^{-0.25}$, where r is the size of the void, I is the coil current, and E_p is the proton energy.[11] Synthetic radiographs are generated for varying coil currents, and experimental coil currents are inferred by overlaying the synthetic images on the experimental data. Using this methodology, coil currents were inferred for the various laser pulse widths to be 17 ± 1, 13 ± 1, 11 ± 1, and 10 ± 1 kA for pulse widths of 2, 3, 4, and 9.9 ns, respectively (see Fig. 5). To illustrate the analysis procedure, raw experimental data, synthetic radiograph, and corresponding overlay are shown in Fig. 4 for $\tau_l = 9.9$ ns, $E_p = 24.7$ MeV. As the coil currents are inferred by comparing

synthetic and experimental data, error bars are defined by the granularity of the prescribed current between successive synthetic radiographs.

Since protons of different energies are deflected differently by electric and magnetic fields, degeneracy in the proton structure can be resolved by performing fits for various proton energies. To confirm the prolate void features are created primarily by the coil magnetic field and not due to electric field, radiographs corresponding to $E_p = 18.3$ MeV and $E_p = 33.1$ MeV are analyzed, in addition to the primary dataset of $E_p = 24.7$ MeV shown in Fig. 2. In all cases, the inferred coil magnetic field was within 1 kA of the 24.7 MeV proton energy case, within measurement error bars.

The data (Fig. 5) demonstrate a clear decline in generated coil current with increasing laser pulse width at constant intensity. The lumped-circuit model in Sec. IV explains this trend.

IV. LUMPED-CIRCUIT MODEL

We built on and applied a lumped-circuit model to characterize the effects of an intense laser pulse on a capacitor-coil target. In this and other lumped-circuit models,[10,12,14] the current through the coil is calculated by modeling the target as a RLC series circuit. The voltage between the plates U is described by the current sources
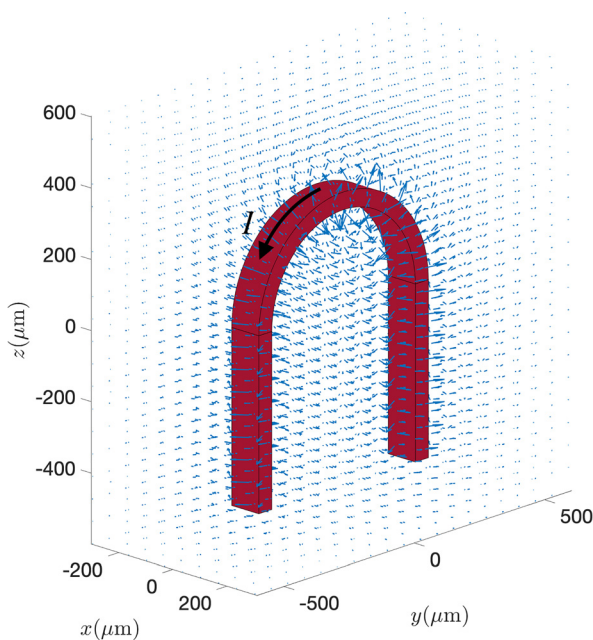

FIG. 3. Simulated magnetic field distribution by a U-shaped coil current. The simulated current matches experimental coil dimensions. Protons from radiography are incident from the y direction.

$$C\frac{dU}{dt} = I_i - I_e + I_c, \qquad (1)$$

where C is the target capacitance, and I_i and I_e are the ion and electron currents produced by the expanding plasma hitting the front plate, respectively, and I_c is the coil current. I_i and I_e are described as time-dependent current sources, as they are caused by the laser interaction with the back plate. The electron current term can be further separated into hot electron and cold electron currents to accommodate a two-temperature model, represented by $I_{e,h}$ and $I_{e,c}$, respectively. Irrespective of temperature, electrons are assumed to be deflected by the accumulation of negative charge on the front plate and the current can be described by a Boltzmann distribution, $I_e = I_{e,h} + I_{e,c} = K_h I_{e0} \exp(U/T_{e,h}) + (1 - K_h)I_{e0}\exp(U/T_{e,c})$. Here, K_h is the fraction of hot electrons relative to the combined electron population, I_{e0} is the initial electron current, and $T_{e,h}$ and $T_{e,c}$ refer to the hot and
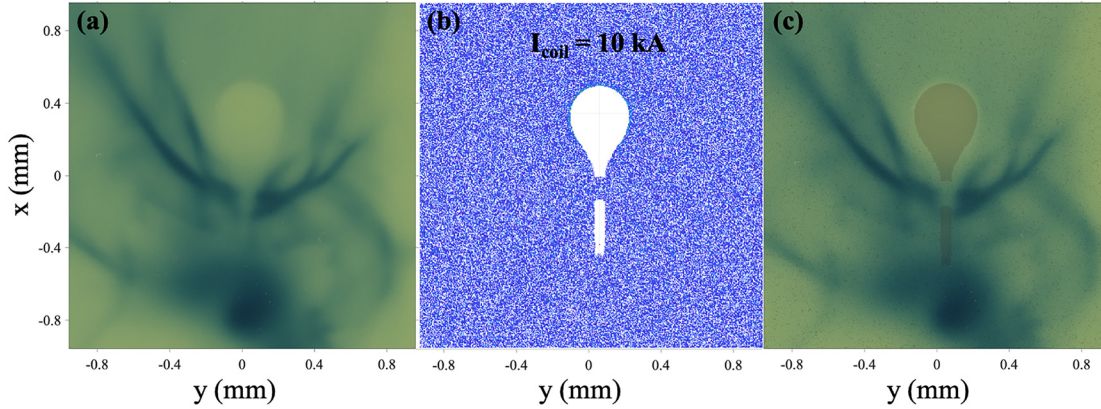
FIG. 4. (a) Experimental proton radiograph, (b) synthetic proton radiograph, and (c) overlay are shown for the shot with laser pulse width $\tau_l = 9.9$ ns, $E_p = 24.7$ MeV. Synthetic radiographs are made for various coil current values. Fits are obtained by creating an image mask based on the simulated proton image and overlaying it on top of the experimental data.

cold electron temperatures, respectively. A density-weighted electron temperature can be defined as the effective temperature,

$$T_{\text{eff}} = T_{e,h} \frac{K_h + \left(1 - K_h \sqrt{T_{e,c}/T_{e,h}}\right)}{K_h + \left(1 - K_h \sqrt{T_{e,h}/T_{e,c}}\right)}, \tag{2}$$

and the ion sound speed c_s is calculated using T_{eff}. The ion current is assumed to follow a self-similar expansion model,[26] $I_i = I_{i0} e^{-d/c_s t}$, where I_{i0} is the initial ion current, c_s is taken as the characteristic ion velocity, and d is the distance between the capacitor plates.

Substituting the expressions for ion and electron currents, Eq. (1) becomes
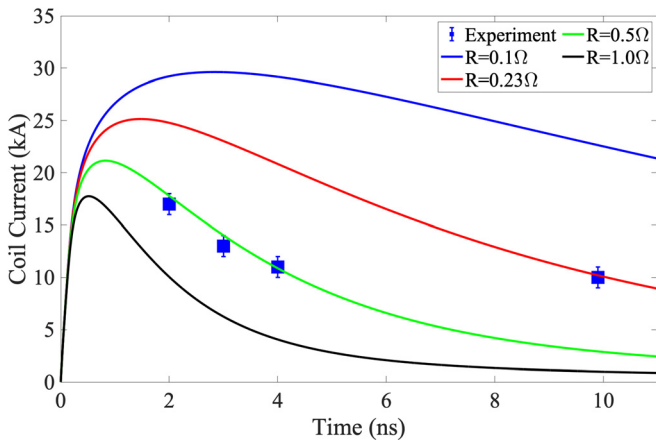

FIG. 5. Lumped-circuit model simulations of coil current as a function of laser pulse duration, compared with experimental measurements. In the mode, resistance is assumed constant for each run, but varied as a free parameter to account for temperature effects. $R = 0.5\,\Omega$ provides the best match to experimental measurements, but diverges at late time. $R = 0.23\,\Omega$ matches the data point at $t = 9.9$ ns. In all cases, coil current is observed to eventually decay with increasing laser pulse width due to ion shorting.

$$C\frac{dU}{dt} = \begin{cases} I_{i0} \exp\left(-d/c_s t\right) - K_h I_{e0} \exp\left(U/T_{e,h}\right) \\ \quad - (1 - K_h) I_{e0} \exp\left(U/T_{e,c}\right) + I_c, \\ \quad 0 < t \le \tau_l \\[8pt] I_{i0} \exp\left(-d/c_s t\right) \exp\left(-(t - \tau_l)/\tau_{d,i}\right) \\ \quad - (K_h I_{e0} \exp\left(U/T_{e,h}\right) \\ \quad + (1 - K_h) I_{e0} \exp\left(U/T_{e,c}\right)) \exp\left(-(t - \tau_l)/\tau_{d,e}\right) + I_c, \\ \quad t > \tau_l. \end{cases} \tag{3}$$

The initial electron term can be estimated as $I_{e0} \sim n_{e0} e (K_h v_{e,h} + (1 - K_h) v_{e,c}) A_{ls}$, where n_{e0} is the electron density (estimated as the critical density n_c for a 3ω beam), e is the elementary charge, $v_{e,h}$ and $v_{e,c}$ are the hot and cold electron velocities, and A_{ls} is a characteristic cross-sectional area, here taken to be the area of the laser spot. To match the steady-state solution at infinite time, assuming $U(t \to \infty) = 0$ and no coil current, $I_{i0} = I_{e0}$. The ion and electron current terms only exist when the laser is on. After laser-shutoff, the ion and electron currents are assumed to exponentially decay with time constants $\tau_{d,i}$ and $\tau_{d,e}$, respectively. It is therefore assumed that soon after the laser pulse is turned off, the voltage between the plates is discharged wholly through the coils.

The behavior of the voltage between the plates can be described by the components of the RLC circuit. Specifically,

$$-U = RI_c + L\frac{dI_c}{dt}. \tag{4}$$

Here, R is the resistance and L is the coil inductance. In general, the circuit parameters R, L, and C are assumed constant, but second-order effects can be incorporated, such as temperature dependence of the resistance. Equations (3) and (4) form a set of coupled differential equations that serve as a model to understand how these currents are generated.

Using this model, simulations are performed using experimental parameters. Electron and ion parameters are assigned as follows: the cold electron temperature $T_{e,c} \sim 5$ keV is inferred from a 2D FLASH simulation of a 1.7×10^{16} W/cm^2 laser hitting a copper target. Hot

electron temperature and hot electron fraction are assumed to follow the scalings in Forslund et al.[21] $K_h = 0.2(I_{las}\lambda_{las}^2/T_{e,c}) \sim 0.13$ and $T_{e,h} = 9(I_{las}\lambda_{las}^2)^{0.25} \sim 10.8$ keV, where I_{las} is the laser intensity in PW/cm^2, λ_{las} is the laser wavelength in μm, and $T_{e,c}$ and $T_{e,h}$ are in keV. With $n_{e0} = n_c[3\omega] = 9 \times 10^{27}$ m^{-3} and $A_{ls} = 8 \times 10^{-9}$ m^{-2}, the initial ion and electron currents are 360 MA. Decay times $\tau_{d,i}$ and $\tau_{d,e}$ are set to 0.1 ns; model results are not sensitive to the decay time, as long as they are subnanosecond timescale. Inductance and capacitance are calculated from the target geometry to be 1.2 nH and 0.1 pF, respectively, and do not change significantly over the course of the interaction. Coil resistance is kept as a free parameter due to its strong temperature dependence: as the coil heats significantly from room temperature to vaporization temperature due to Ohmic heating, the resistivity increases by roughly a factor of 10. A more complete, self-consistent model would include a full treatment of the time-dependent temperature and therefore account for wire resistance changes during the laser pulse, but in our analysis, we recognize this effect by running the lumped-circuit model with constant, but varied resistance values.

Results from the lumped-circuit model, combined with the experimental measurements, are shown in Fig. 5. Multiple model runs are shown, demonstrating a range of wire resistance values. Since the coil current values are measured at the end of the laser pulse, these plots also represent the time evolution of the coil current, up to the end of the laser pulse duration. Overall, the model results show that as laser pulse width increases, current coil initially rises, reaches a peak at some time t_{max}, and subsequently falls. The decline in current is due to the arrival of ions reaching the front plate, which effectively shorts out the circuit. This phenomenon occurs on a timescale similar to the "ion transit time" $\tau_i \sim d/v_{ion}$, where v_{ion} is preliminarily taken to be the sound speed c_s. In our specific case, $d = 600 \mu$m, $c_s = 3.9 \times 10^5$ m/s, so $\tau_i = 1.5$ ns. If the laser pulse width is shorter than τ_i, the coil current is seen to rise up until the end of the laser pulse, only decaying after laser turn-off. As the laser pulse width grows comparable to and beyond the transit time, the coil current is seen to decay while the laser pulse is still on due to the ion arrival.

To further demonstrate that the ion transit time is the primary factor in determining coil current behavior for long pulse widths, the ion transit speed v_{ion} is artificially varied from c_s (Fig. 6). In these runs, the laser pulse width is set longer than the probe time of 10 ns, so the laser source is on for the entire interaction. The onset of coil current decay is characterized by the time of peak current t_{max}. As the ion velocity is decreased, t_{max} is delayed, due to a longer ion transit time. If the onset of current decay is affected only by the ion transit time, the expected dependence is $t_{max} = d/v_{ion} \propto v_{ion}^{-1}$. To analyze the model, a power-law is fit for various imposed values of v_{ion}; an index of -0.74 is found. This dependence is weaker than the expected index of -1, but it is readily explained by the presence of other damping terms in the model. Resistance and inductance act similarly to the ion current term as effective current drains, so the ion shorting time alone does not define t_{max}.

A. FLASH simulations and time-dependent effects in the lumped-circuit model

Previously, we developed a lumped-circuit model to describe the dependence of coil current on laser pulse width. It is observed that the ion transit time plays a critical role in determining the peak of the current profile, but there are other factors in the model that prevent a
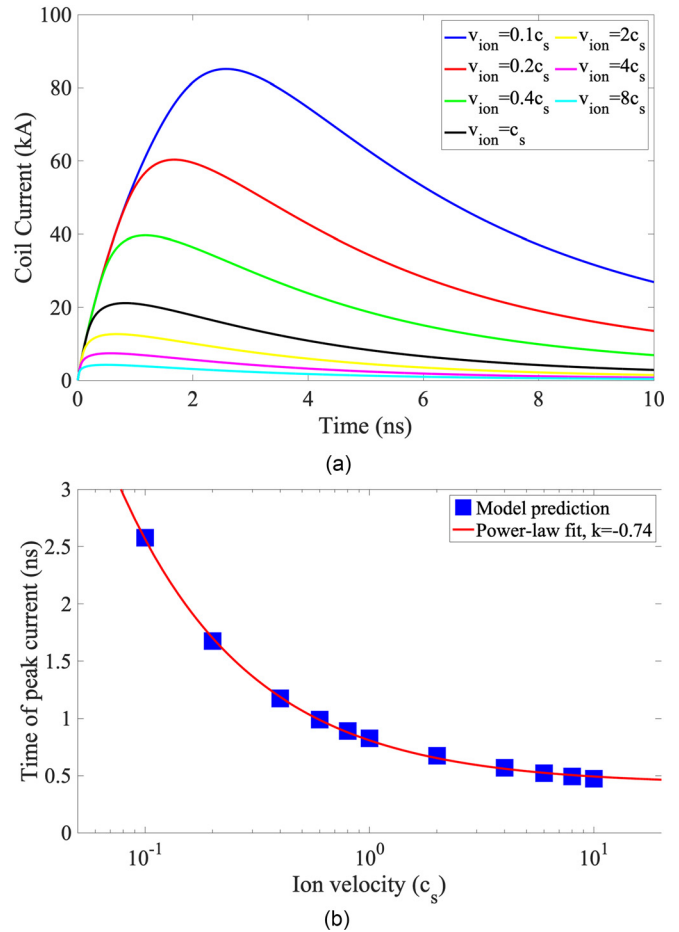

FIG. 6. (a) Time evolution of coil current for varying values of ion velocity. The laser is on for the duration of the runs. Onset of coil current decay occurs earlier in time for larger ion velocity, corresponding to a smaller ion transit time. $R = 0.5\,\Omega$ is assumed for all runs. (b) Power law with index –0.74 is fit to time of peak current t_{max} vs ion velocity v_{ion}.

complete and accurate prediction. In comparing the experimental data with results from the model, good agreement is achieved for the data points at 2, 3, and 4 ns with an assumed coil resistance of $R = 0.5\,\Omega$. However, the measured coil current at 9.9 ns is significantly larger than the model prediction. To predict the measured coil current at 9.9 ns, a coil resistance of $R = 0.23\,\Omega$ must be used, but in turn, this value significantly overestimates the coil currents at earlier times.

This discrepancy can be explained by the inaccurate assumption of constant resistance. In a simple model of resistance through a wire, resistivity ρ and skin depth δ are the primary time-dependent factors that affect the bulk resistance value: $R = \rho L/A$, where L is the length of the wire and A is the cross-sectional area of current flow. Resistivity is assumed to scale linearly with temperature,

$$\rho(T) = \rho_0(1 + \alpha(T - T_0)), \qquad (5)$$

where $\rho_0 = 1.68 \times 10^{-8}\,\Omega$ m is the Cu resistivity at 300 K, $\alpha = 0.003\,93$ K^{-1} is the temperature scaling factor, T is the temperature,

and $T_0 = 300$ K. The rectangular wire cross-sectional area measures $100 \, \mu m \times 50 \, \mu m$, and assuming skin depth is uniform from the boundary in both dimensions, a geometric value for cross-sectional area can be obtained, $A \sim (300 \, \mu m) \delta - 4\delta^2$. Skin depth is assumed to increase with increasing laser pulse duration, as $\delta = (2\rho/\omega\mu)^{0.5}$,[27] and $\omega \sim \pi/\tau_l$. The resistivity and skin effects are therefore competing factors, with the former contributing to a resistance increase as the wire is heated, and the latter contributing to a resistance decrease as the effective cross-sectional area of current flow is increased.

2-D FLASH[28,29] radiative MHD simulations were performed to model the temperature and skin effect evolution with time. The simulation employed the high energy density physics capabilities, including laser ray-tracing, three-temperature hydrodynamics, tabulated EOS and opacity model from IONMIX,[30] grouped radiation transportation, Spitzer thermal conductivity with flux limiter (f = 0.06), and the resistive MHD model.[31] This simulation was conducted in 2D (x-y plane) Cartesian coordinates with a $10 \, \mu m$-resolution uniform grid, and the initial density and laser deposition profiles are shown in Fig. 7. The simulation uses a $100 \, \mu m \times 50 \, \mu m$ wire at $y = 1.6$ mm to represent the coil along the z-direction crossing the simulation plane. The electric field (1.75×10^7 V/m) along the wire was applied in the region where density exceeds 0.1 g/cc for the first 0.8 ns. This field strength corresponds to a 35 kV voltage over the 2 mm coil length. The resistivity of the wire is modeled by connecting the linear temperature scaling Eq. (5) to the Spitzer resistivity at 50 eV, suggested by the measured Al resistivity model.[32] Spitzer resistivity is used in the plasma. The resulting current evolution matches the experimental current profile.

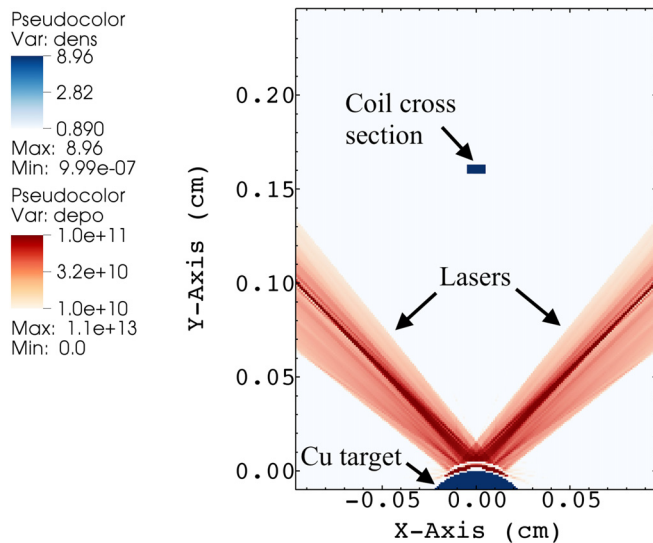In addition to current and field generation, this simulation modeled the plasma behavior and radiation from the laser-capacitor interaction.[16] The physics of the laser-generated plasma colliding with the coil-generated plasma and radiative heating of the coil surface are captured. Due to the lack of a third spatial dimension, we approximated experimental conditions by two laser beams interacting with a circular Cu region with a radius of 0.3 mm, positioned 1.55 mm below the coil. Laser intensity of 4×10^{14} W/cm^2 and a $100 \, \mu m$ radius spot with a 0.3 ns pulse duration were prescribed for both beams. These laser parameters were chosen to match the experimental time at which the laser-generated plasma collides with the coil-generated plasma of 1.0 ns. A 3D MHD simulation replicating the experimental geometry would improve the modeling of the capacitor coil target; however, this 2D simulation is sufficient to demonstrate the coil skin effect and temperature evolution.

Current density and temperature profiles were taken from the simulation at 2, 3, and 4 ns. Skin depth was obtained by integrating the current density along the $100 \, \mu m$ width of the wire and defined as the distance from the edge where 68% of the total wire current is located. A representative temperature is then taken at the skin depth location and used to calculate resistivity. The time evolution of resistivity and skin depth from the simulations are shown in Fig. 8. As expected, resistivity and skin depth both increase with time, with a stronger rise observed in resistivity. The resulting effect on bulk resistance is also an increase from $0.060 \, \Omega$ to $0.11 \, \Omega$, at 2 ns and 4 ns, respecively, with $R_{3 \, ns}/R_{2 \, ns} \sim 1.3$ and $R_{4 \, ns}/R_{2 \, ns} \sim 1.8$.

V. DISCUSSION

A. Parameter scan of v_{ion}, $T_{e,h}$ to infer coil resistance

The observed trend from Sec. IV A can be used to analyze the lumped-circuit model and constrain certain free parameters, particularly hot electron temperature $T_{e,h}$ and ion velocity v_{ion}. An extensive scan of these parameters is performed by setting values for $T_{e,h}$ and v_{ion} and inferring a resistance R_{inf} that results in the model matching the experimental measurements at various times. A number of hot

FIG. 7. Initial density and laser deposition profiles used in the FLASH simulations. An out-of-plane electric field of 1.75×10^7 V/m is prescribed in the coil cross section for 0.8 ns to generate the magnetic field. Two laser beams of intensity 4×10^{14} W/cm^2 drive a separate Cu target for 0.3 ns to simulate the laser-generated plasma in the experiment. Laser and electric field timings are chosen to match the collision of laser-generated and coil-generated plasma plumes at 1.0 ns, as observed experimentally.
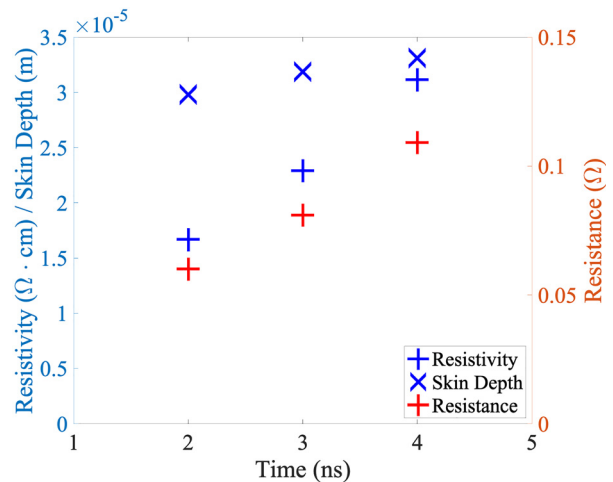

FIG. 8. Resistivity (blue plus), skin depth (blue cross), and resistance (red plus) are plotted as a function of time, based on FLASH simulations. Resistivity is seen to rise more sharply than skin depth, due to the linear temperature dependence of resistivity. Combining both time-dependent effects results in a bulk resistance increase with time.

electron temperature scalings are shown, as well as an upper limit of 50 keV. This upper limit was established by an earlier experiment on OMEGA EP, where the hot electron temperature was measured with a similar laser interaction, but with 1.8 times the laser intensity. v_{ion} was scanned from subsonic velocities up to a few times ion sound speed (Fig. 9). A lower bound on hot electron temperature is taken to be the cold electron temperature $T_{e,c} = 5$ keV.

The earlier FLASH simulations established an increasing trend in resistance from 2 ns to 4 ns (Fig. 8). Across the range of assumed hot-electron temperatures, a decrease in resistance over time is observed for subsonic and sonic ion velocities. As ion velocity is increased, the time derivative of resistance is seen to trend positive. In addition, the positive $\frac{dR}{dt}$ behavior is more pronounced for lower hot electron temperatures. For instance, for $v_{ion} = 2c_s$, inferred resistances corresponding to $T_{e,h} = 10.8$ keV and $T_{e,h} = 13.9$ keV increase with time, from $0.1\,\Omega$ to $0.25\,\Omega$ and from $0.2\,\Omega$ to $0.3\,\Omega$, respectively. On the other hand, for higher electron temperatures of $T_{e,h} = 27.6$ keV and

$T_{e,h} = 50$ keV, the trend reverses, and the inferred resistances decrease with time, from $0.5\,\Omega$ to $0.43\,\Omega$ and from $0.77\,\Omega$ to $0.54\,\Omega$, respectively. From this observation on the slope of the resistance, it is then possible to constrain hot electron temperature as a function of ion velocity: for a given ion velocity, the hot electron temperature below which the inferred resistance begins to trend positively with time is an upper bound. This constraint is represented by the red line in Fig. 10.

A lower bound constraint can also be established. For a given ion velocity, a certain hot electron temperature is needed to match the experimentally measured coil current. Setting the resistance to zero (0) provides the minimum hot electron temperature as a function of ion velocity. This is represented by the blue line in Fig. 10.

Combining the previously discussed constraints, a limited area of possible $(T_{e,h}, v_{ion})$ pairs can be found. It can be seen that a subsonic or sonic ion speed is unlikely: $T_{e,h}$ would need to be very low, only slightly above $T_{e,c}$. For larger ion speeds, the corresponding allowed
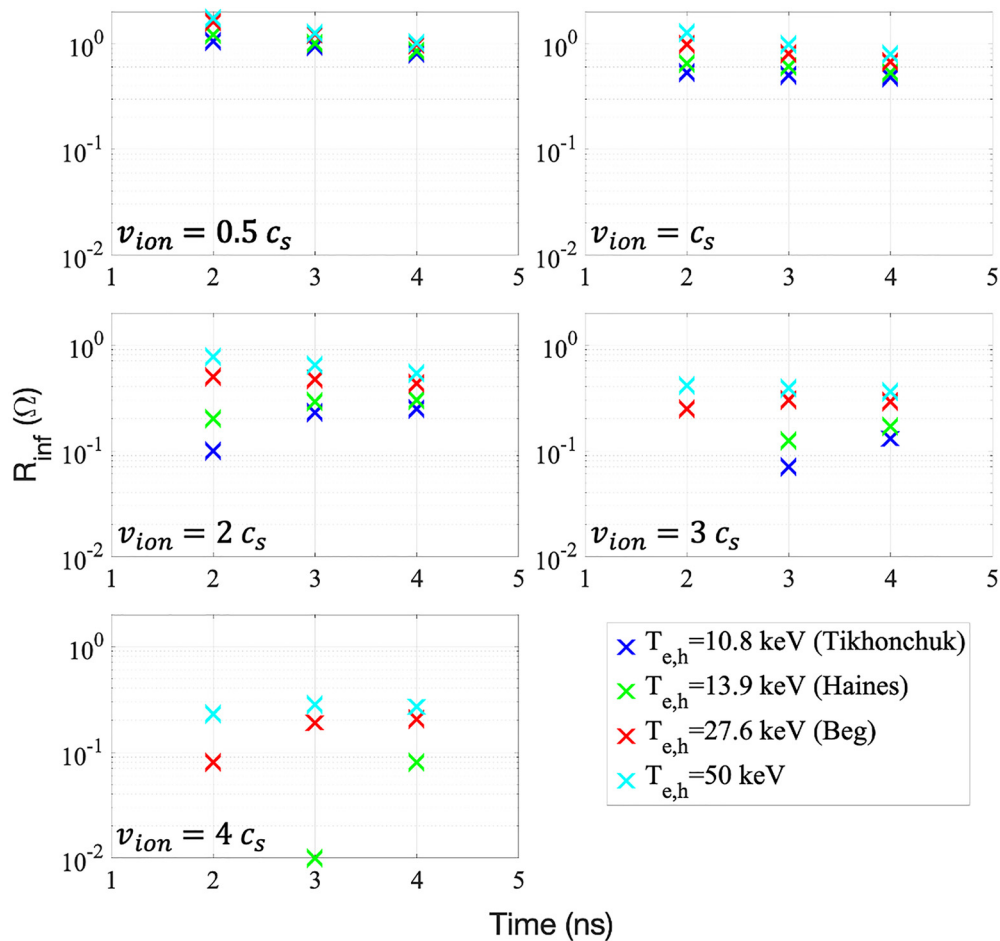

FIG. 9. An extensive parameter scan is performed by varying v_{ion} and $T_{e,h}$. By fixing these free parameters, a resistance is inferred for each time by comparing lumped-circuit model predictions with experimental measurements. For low ion velocities and across all hot-electron temperatures, the inferred resistance decreases with increasing time, contradicting the trend predicted by FLASH simulations. As ion velocity grows past the ion sound speed, the resistance trend reverses to increase with time. (Note: Missing data points for high ion velocities and low electron temperatures are due to implied resistance values of 0, which cannot be plotted on a logarithmic scale. In these situations, the ion shorting effect is sufficiently strong that even with 0 wire resistance, there is insufficient electron current drive to achieve the experimental current.)
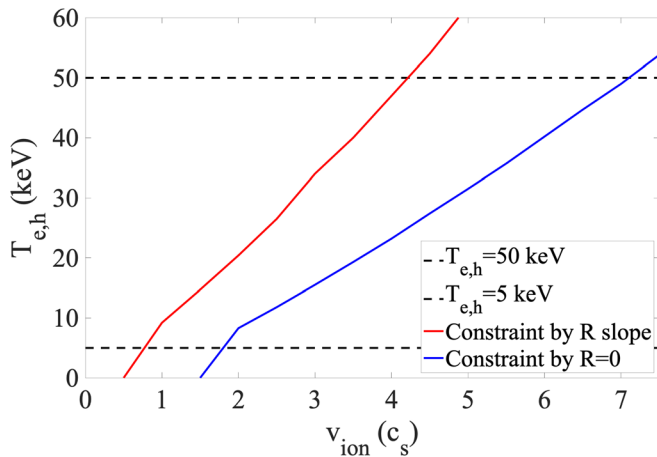
FIG. 10. A representation in phase-space of possible hot-electron temperatures and ion velocity, constrained by the lumped-circuit model. Horizontal dashed lines represent constant upper and lower bounds. The upper bound of 50 keV is an experimental bound from an earlier experiment, where 45 to 50 keV hot electrons were measured with 1.8-time higher laser intensity. The lower bound is established by the bulk electron temperature of ∼5 keV. The red line upper bound is constrained by the requirement that the resistance must increase with time from 2 ns to 4 ns. The blue line lower bound is derived from a minimum hot electron temperature needed to achieve experimental coil currents, at 0 resistance.

hot-electron temperatures to grow as well. At a reasonable $T_{e,h}$ = 30 keV, $v_{ion} \sim 3$–4.5 c_s. Due to the experimental upper limit of 50 keV, ion velocity is also unlikely to exceed 7.5 c_s. In addition, FLASH simulations (Fig. 8) infer a resistance of ∼0.1 Ω within this time frame. Comparing the calculated resistance with the inferred resistance values from Fig. 9, the best match occurs at $v_{ion} \sim 3$–4 c_s. While no definitive conclusions can be drawn, these results from the lumped-circuit model provide a useful basis: with additional experiments and measurements of hot electron population temperatures, the predictions from the model can be better understood and constrained.

B. Outer bubble feature

In addition to the inner prolate feature produced by the magnetic field deflection, an outer bubble feature is observed in the proton radiographs at $t = 2$, 3, and 4 ns. This feature is also observed in previous proton radiograph data involving laser-driven capacitor coils.[11]

The inner and outer features can be explained by the coil current and return current, respectively. Using the FLASH simulation described in Sec. IV A, a synthetic proton radiograph is calculated from the field structure by calculating the deflection angle and distances [Fig. 11(a)]. The synthetic image shows good agreement with the experimental radiograph in Fig. 2, importantly having two well-defined bubble features (labeled points C and D).

Vertical lineouts of the proton radiograph signal, deflection distance, and J_z are taken at $x = 0$ [Fig. 11(c)]. Caustics are formed when the spatial derivative of the deflection distance equals −1: $\mathrm{d}(d_{\mathrm{def}})/\mathrm{d}y = -1$. This is due to a group of protons from the local area all being deflected onto the same spot, forming a sharp concentration of protons. Spikes in the proton lineout are labeled A–D, with the corresponding locations in the deflection lineout marked accordingly.
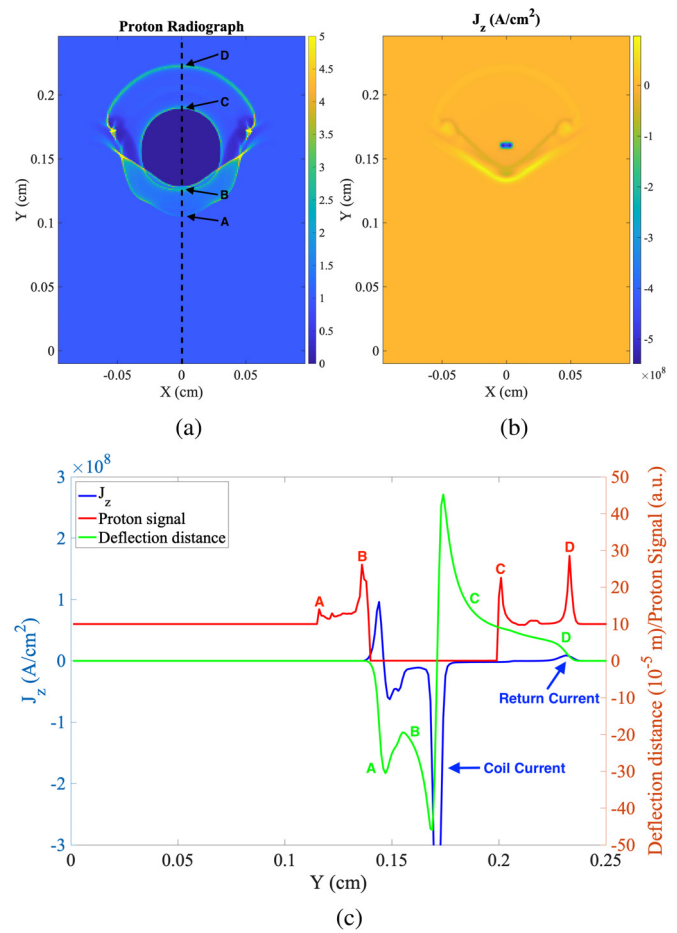

(a)   (b)

(c)

FIG. 11. FLASH simulations of an out-of-plane current at 2 ns. (a) A synthetic proton radiograph is calculated from the local electromagnetic fields. Inner and outer features are observed (labeled C and D, respectively) in the radiograph. Additional caustics (A and B) are also labeled. (b) The out-of-plane current J_z shows a dark blue spot representing the coil current and a light yellow semicircular structure corresponding to the return current. (c) Centered vertical lineouts of the out-of-plane current, proton radiograph signal, and proton deflection distance are shown. Caustic locations marked in the proton radiograph are labeled in the proton signal lineout (red). The corresponding locations where the deflection plot (green) has a slope of −1, thus forming the caustic, are shown. The primary inner and outer features are shown to be caused by the coil current and return current, respectively, shown in the J_z lineout (blue). (a) Simulated proton radiograph, (b) Out-of-plane current J_z, and (c) Vertical lineouts at $X = 0$ (dashed line) of J_z, proton radiograph signal, and deflection distance due to the magnetic field.

Points C and D, corresponding to the boundaries of the inner and outer void features, are caused by the coil current and return current, respectively, as seen in the J_z lineout. For the simple case of a current-carrying wire in a vacuum, the magnetic field decays as $1/r$ from the wire center. The deflection distance also decays as $1/r$, creating exactly one point where the slope is −1, and therefore, one caustic feature. In contrast, because of the presence of a plasma, there is a return current, which creates an inflection point in the magnetic field decay profile. An additional point is created where the slope is −1, creating the second outer feature.

VI. CONCLUSIONS

We experimentally investigate the effects of laser pulse width on the generated current in a capacitor-coil target for a fixed laser intensity. Proton radiography measurements of the magnetic field at the end of the laser pulse for various pulse widths provide a temporal evolution of the coil current while the laser is on. The measurements taken at 2, 3, 4, and 9.9 ns indicate a decrease in coil current with increasing pulse width.

A lumped-circuit model was created to analyze and explain the experimental results. In the model, we assumed a two-temperature electron population and an ion population that follows a self-similar expansion model with ion velocity equal to the sound speed. Resistance was kept as a free parameter to account for the temperature dependence of resistivity and skin effect within the wire. Good agreement with experimental data was found for measurements at 2, 3, and 4 ns with resistance $R = 0.5\Omega$, but the model significantly underestimated coil current at 9.9 ns. It was found that current decay with increasing laser pulse width was due to the arrival of the ion current at the front plate, or "ion shorting." The time of maximum coil current is found to depend on the ion velocity as $t_{max} \propto v_{ion}^{-0.74}$. This dependence is not as strong as the expected inverse relation from assuming $t_{max} \sim t_{ion} = d/v_{ion}$. The discrepancy can be explained by the inherent resistive effects in the circuit. Nevertheless, the strong scaling provides further evidence of the ion shorting effect.

The time-dependence of resistivity and the skin effect was investigated with 2-D FLASH simulations. From 2 to 4 ns, it was found that resistivity and skin depth both increased with time, resulting in an increasing bulk resistance with time as well. The obtained trend was applied to an extensive parameter scan of v_{ion} and $T_{e,h}$ to constrain hot electron temperature and ion speeds. Ion velocity is likely supersonic but does not exceed $7.5\,c_s$, and hot electron temperature values are further bounded by the chosen ion velocity. Additional comparisons of the calculated resistance values from FLASH simulations and the lumped-circuit model imply an ion speed in the middle of the range: $\sim$3–4 c_s.

An additional outer feature was observed in the proton radiography data at $t = 2, 3$, and 4 ns. A synthetic proton radiograph based on FLASH simulations reproduced the experimental feature: a return current carried by the plasma outside the wire was found to be the cause for the outer feature. The absence of the outer feature at late time is due to low plasma density; the return current at the time is insufficient to produce the additional feature.

The behavior of capacitor-coils is nuanced and highly dependent on laser parameters and plasma conditions. For instance, the ion shorting effect shown in this paper was not observed in other similar studies.[18] This is likely due to the different laser energy regimes of the two studies, which can significantly affect plasma dynamics between the capacitor plates, as well as the behavior of the coil current. Future studies can improve the lumped-circuit model to incorporate time-dependent effects. More complete experimental data can also further constrain free parameters and resolve assumptions to the existing model. Such improved models can connect these higher laser intensity regimes to low laser power, along with experimental confirmation of this transition.

ACKNOWLEDGMENTS

DATA AVAILABILITY

The data that support the findings of this study are available from the corresponding author upon reasonable request.

REFERENCES

[1]M. Hohenberger, P.-Y. Chang, G. Fiksel, J. P. Knauer, R. Betti, F. J. Marshall, D. D. Meyerhofer, F. H. Séguin, and R. D. Petrasso, Phys. Plasmas **19**, 056306 (2012).

[2]X. X. Pei, J. Y. Zhong, Y. Sakawa, Z. Zhang, K. Zhang, H. G. Wei, Y. T. Li, Y. F. Li, B. J. Zhu, T. Sano, Y. Hara, S. Kondo, S. Fujioka, G. Y. Liang, F. L. Wang, and G. Zhao, Phys. Plasmas **23**, 032125 (2016).

[3]A. Chien, L. Gao, H. Ji, X. Yuan, E. G. Blackman, H. Chen, P. C. Efthimion, G. Fiksel, D. H. Froula, K. W. Hill, K. Huang, Q. Lu, J. D. Moody, and P. M. Nilson, Phys. Plasmas **26**, 062113 (2019).

[4]N. C. Woolsey, Y. A. Ali, R. G. Evans, R. A. D. Grundy, S. J. Pestehe, P. G. Carolan, N. J. Conway, R. O. Dendy, P. Helander, K. G. McClements, J. G. Kirk, P. A. Norreys, M. M. Notley, and S. J. Rose, Phys. Plasmas **8**, 2439 (2001).

[5]L. J. Perkins, B. G. Logan, G. B. Zimmerman, and C. J. Werner, Phys. Plasmas **20**, 072708 (2013).

[6]V. Korobkin, Sov. Tech. Phys. Lett. **5**, 474 (1979).

[7]J. F. Seely, Appl. Phys. B **31**, 37 (1983).

[8]H. Daido, F. Miki, K. Mima, M. Fujita, K. Sawai, H. Fujita, Y. Kitagawa, S. Nakai, and C. Yamanaka, Phys. Rev. Lett. **56**, 846 (1986).

[9]S. Fujioka, Z. Zhang, K. Ishihara, K. Shigemori, Y. Hironaka, T. Johzaki, A. Sunahara, N. Yamamoto, H. Nakashima, T. Watanabe, H. Shiraga, H. Nishimura, and H. Azechi, Sci. Rep. **3**, 1–7 (2013).

[10]C. Courtois, A. D. Ash, D. M. Chambers, R. A. D. Grundy, and N. C. Woolsey, J. Appl. Phys. **98**, 054913 (2005).

[11]L. Gao, H. Ji, G. Fiksel, W. Fox, M. Evans, and N. Alfonso, Phys. Plasmas **23**, 043106 (2016).

[12]G. Fiksel, W. Fox, L. Gao, and H. Ji, Appl. Phys. Lett. **109**, 134103 (2016).

[13]C. Goyon, B. B. Pollock, D. P. Turnbull, A. Hazi, L. Divol, W. A. Farmer, D. Haberberger, J. Javedani, A. J. Johnson, A. Kemp, M. C. Levy, B. G. Logan, D. A. Mariscal, O. L. Landen, S. Patankar, J. S. Ross, A. M. Rubenchik, G. F. Swadling, G. J. Williams, S. Fujioka, K. F. F. Law, and J. D. Moody, Phys. Rev. E **95**, 033208 (2017).

[14]V. T. Tikhonchuk, M. Bailly-Grandvaux, J. J. Santos, and A. Poyé, Phys. Rev. E **96**, 023202 (2017).

[15]X. Yuan, J. Zhong, Z. Zhang, W. Zhou, J. Teng, Y. Li, B. Han, D. Yuan, J. Lin, C. Liu, Y. Li, B. Zhu, H. Wei, G. Liang, W. Hong, S. He, S. Yang, Y. Zhao, Z. Deng, F. Lu, Z. Zhang, B. Zhu, K. Zhou, J. Su, Z. Zhao, Y. Gu, G. Zhao, and J. Zhang, Plasma Phys. Controlled Fusion **60**, 065009 (2018).

[16]J. L. Peebles, J. R. Davies, D. H. Barnak, T. Cracium, M. J. Bonino, and R. Betti, Phys. Plasmas **27**, 063109 (2020).

[17]V. V. Ivanov, A. V. Maximov, A. L. Astanovitskiy, I. A. Begishev, R. Betti, J. R. Davies, C. Mileham, J. D. Moody, C. Stoeckl, K. J. Swanson, N. L. Wong, and J. Bromage, Phys. Plasmas **27**, 033102 (2020).

[18]G. J. Williams, S. Patankar, D. A. Mariscal, V. T. Tikhonchuk, J. D. Bude, C. W. Carr, C. Goyon, M. A. Norton, B. B. Pollock, A. M. Rubenchik, G. F. Swadling, E. R. Tubman, and J. D. Moody, J. Appl. Phys. **127**, 083302 (2020).

[19]J. J. Santos, M. Bailly-Grandvaux, L. Giuffrida, P. Forestier-Colleoni, S. Fujioka, Z. Zhang, P. Korneev, R. Bouillaud, S. Dorard, D. Batani, M. Chevrot, J. E. Cross, R. Crowston, J.-L. Dubois, J. Gazave, G. Gregori, E. d'Humières, S.

Hulin, K. Ishihara, S. Kojima, E. Loyez, J.-R. Marquès, A. Morace, P. Nicolaï, O. Peyrusse, A. Poyé, D. Raffestin, J. Ribolzi, M. Roth, G. Schaumann, F. Serres, V. T. Tikhonchuk, P. Vacar, and N. Woolsey, New J. Phys. **17**, 083051 (2015).

[20]K. F. F. Law, M. Bailly-Grandvaux, A. Morace, S. Sakata, K. Matsuo, S. Kojima, S. Lee, X. Vaisseau, Y. Arikawa, A. Yogo, K. Kondo, Z. Zhang, C. Bellei, J. J. Santos, S. Fujioka, and H. Azechi, Appl. Phys. Lett. **108**, 091104 (2016).

[21]D. W. Forslund, J. M. Kindel, and K. Lee, Phys. Rev. Lett. **39**, 284 (1977).

[22]J. S. Pearlman and G. H. Dahlbacka, Appl. Phys. Lett. **31**, 414 (1977).

[23]A. Tarifeño, C. Pavez, and L. Soto, J. Phys.: Conf. Ser. **134**, 012048 (2008).

[24]S. C. Wilks, A. B. Langdon, T. E. Cowan, M. Roth, M. Singh, S. Hatchett, M. H. Key, D. Pennington, A. MacKinnon, and R. A. Snavely, Phys. Plasmas **8**, 542 (2001).

[25]L. Gao, P. M. Nilson, I. V. Igumenshchev, M. G. Haines, D. H. Froula, R. Betti, and D. D. Meyerhofer, Phys. Rev. Lett. **114**, 215003 (2015).

[26]P. Mora, Phys. Rev. Lett. **90**, 185002 (2003).

[27]T. Vijayan and V. K. Rohatgi, J. Appl. Phys. **63**, 2576 (1988).

[28]B. Fryxell, K. Olson, P. Ricker, F. X. Timmes, M. Zingale, D. Q. Lamb, P. MacNeice, R. Rosner, J. W. Truran, and H. Tufo, Astrophys. J. Suppl. Ser. **131**, 273 (2000).

[29]A. Dubey, K. Antypas, M. K. Ganapathy, L. B. Reid, K. Riley, D. Sheeler, A. Siegel, and K. Weide, Parallel Comput. **35**, 512 (2009).

[30]J. Macfarlane, Comput. Phys. Commun. **56**, 259 (1989).

[31]P. Tzeferacos, M. Fatenejad, N. Flocke, C. Graziani, G. Gregori, D. Lamb, D. Lee, J. Meinecke, A. Scopatz, and K. Weide, High Energy Density Phys. **17**, 24 (2015).

[32]H. M. Milchberg, R. R. Freeman, S. C. Davey, and R. M. More, Phys. Rev. Lett. **61**, 2364 (1988).